Three-Dimensional Spatio-Temporal Features for Fast Content-based Retrieval of Focal Liver Lesions

Sharmili Roy*, Yanling Chi, Jimin Liu, Sudhakar K. Venkatesh, and Michael S. Brown

Abstract—Content-based image retrieval (CBIR) systems for three-dimensional (3D) medical datasets still largely rely on two-dimensional (2D) image-based features extracted from a few representative slices of the image stack. Most 2D features that are currently used in the literature not only model a 3D tumor incompletely but are also highly expensive in terms of computation time, especially for high resolution datasets. Radiologist-specified semantic labels are sometimes used along with image-based 2D features to improve the retrieval performance. Since radiological labels show large inter-user variability, are often un-structured, and require user interaction, their use as lesion characterizing features is highly subjective, tedious and slow. In this paper, we propose a 3D image-based spatio-temporal feature extraction framework for fast content-based retrieval of focal liver lesions. All the features are computer-generated and are extracted from 4-phase abdominal CT images. Retrieval performance and query processing times for the proposed framework is evaluated on a database of 44 hepatic lesions comprising of five pathological types. Bull's eye percentage score above 85% is achieved for three out of the five lesion pathologies and for 98% of query lesions, at least one same type of lesion is ranked among the top two retrieved results. Experiments show that the proposed system's query processing is more than 20 times faster than other already published systems that use 2D features. With fast computation time and high retrieval accuracy, the proposed system has the potential to be used as an assistant to radiologists for routine hepatic tumor diagnosis.

Index Terms—3D spatio-temporal focal liver lesion representation, content-based image retrieval, clinical decision support system.

I. INTRODUCTION

FOCAL lesion in the liver refers to a region of different echogenicity, attenuation or signal intensity compared to surrounding liver parenchyma on ultrasound, computed tomography (CT) and magnetic resonance imaging (MRI) respectively and can be of different pathologies. Multi-phase contrast-enhanced computed tomography is the primary imaging technique employed for the detection and characterization

*S. Roy and M. S. Brown are with the Department of Computer Science, National University of Singapore, Singapore 117417 e-mail:(sharmili@comp.nus.edu.sg, brown@comp.nus.edu.sg). Y. Chi and J. Liu are with the Singapore Bioimaging Consortium, Agency for Science, Technology and Research, Singapore 138671 e-mail:(chi_yanling@sbic.a-star.edu.sg, liujm@sbic.a-star.edu.sg). S.K.Venkatesh is with Department of Radiology, Mayo Clinic College of Medicine, Rochester, MN 55905, USA email:(venkatesh.sudhakar@mayo.edu).

of focal liver lesions (FLLs) [1], [2], [3], [4], [5]. The ability to detect and accurately characterize FLLs by qualitative visual inspection comes with years of training and experience and hence is frequently dependent on who is performing the diagnosis. Content-based image retrieval (CBIR) systems are finding increasing use as diagnostic decision support systems. CBIR systems assist radiological diagnosis by searching and retrieving from databases of medical exams and reports confirmed cases that have image features similar to the case under investigation [6], [7], [8].

It has been clinically observed that FLLs exhibit different visual characteristics at various time points after intravenous contrast injection. This evolution of visual features over time carry important diagnostic information and greatly influences FLL classification. Multi-phase contrast-enhanced CT procedure captures this transition by performing consecutive CT scans before and after injection of contrast. A non-contrast enhanced (NC) phase scan is usually performed before contrast injection. The patient then receives intravenous contrast injection and three or more scans are obtained in the arterial (ART) phase (typically 25-40 seconds after start of injection), portal venous (PV) phase (60-75 seconds) and delayed (DL) phase (3-5 minutes). Diffusion of the contrast media over the different phases enhances the vessels and the lesion tissues thereby assisting in lesion type determination.

Classification of liver lesions using image-based features is an active research area. Some studies have reported texture-based classification of lesions in non-enhanced CT and ultra-sonography images using techniques like neural networks [9] and fuzzy support vector machines [10]. In [11], authors provide a comprehensive performance comparison of various texture-based classifier architectures and conclude that a voting-based combination of three primary classifiers gives best classification results. Yu *et al.* in [12] developed a CBIR system to differentiate three types of hepatic lesions using global features derived from non-tensor product wavelet filter and local features based on image density and texture. However, clinical experience shows that non-enhanced CT captures limited diagnostic information. The enhancement patterns observed during various phases of contrast-enhanced images are fundamental for identifying specific focal lesions.

Some published studies have reported characterization of FLLs using multi-phase features. In [13] authors use spatially partitioned bag of visual words (BoW) and intensity, texture and shape-based features derived from a few representative triple-phase image slices to differentiate three lesion types. The features are averaged over all phases which leads to loss of temporal enhancement information. The mean average

precision of the retrieval system is reported to be 88%. In another study by the same group, the BoW-based method is improved to obtain a precision of above 90% using a different set of lesions [14]. A CBIR framework is proposed in [15] to characterize six types of hepatic tumors using multi-phase density and texture features. The texture features are averaged over a bounding box around the tumor and tracked over multiple phases. A "Bull's Eye Percentage" (BEP) score of 78% is achieved. We provide a more detailed comparison of our method with [13], [14], [15] in section IV-A.

In [16], authors use semantic features annotated by radiologists and image features derived from three orthogonal two-dimensional (2D) planes of a single phase CT image to train a random forest classifier that distinguishes benign from malignant tumors in a retrieval framework. The framework is used to characterize sub-centimeter liver lesions. Sub-centimeter lesions are often found indistinguishable in clinical practice and hence are left unclassified though closely monitored. Further, authors in [16] neglect tumor temporal characteristics while designing their features. Napel *et al.* in [17] use high level radiological semantic features and single phase texture and boundary features to characterize three lesion types. Semantic features are unstructured subjective descriptions made by radiologists and are known to exhibit large inter-user variation [18], [19]. Hence, utilization of semantic features in image retrieval may be closely tied to the clinical set-up for which the system is designed.

The CBIR systems discussed thus far represent FLLs using 2D features derived from a few representative slices of the entire exam stack. Physiologically, however, FLLs are three-dimensional (3D) volumes. Hence, 2D features derived from a few slices is clearly an incomplete tumor representation. Further, 2D features may not be representative of the whole lesion, especially in cases of large and heterogenous lesions. Medical image retrieval systems based on 3D features have not been reported extensively in the literature. This is mainly due to the high computation time for 3D features, especially when retrieving high resolution datasets. In [15] authors represent 3D liver lesions by averaging 2D texture features extracted from all the slices where the lesion is visible. Slice-by-slice 2D features only capture structures from the surface. Thus, spatial structural information interlaced within the volume is lost. Linear binary pattern (LBP) extracted from three orthogonal 2D planes have been used to approximate 3D features for fast retrieval of brain lesions in [20]. Again, by modeling the lesions using only three image slices significant part of the lesion volume is neglected. In [21] authors use 3D LBP-based texture bags to retrieve lung lesions. Feature computation time, however, is not reported.

In this paper we propose a fast content-based retrieval framework for FLLs based on 3D spatio-temporal features derived from 4-phase CT scans. All the features are computer generated; no radiological labels are used. The proposed retrieval framework identifies FLLs automatically and aligns the lesions in the four phases using an automated registration pipeline. Regional image-based features are computed from spatially partitioned lesion volumes and tracked over the four phases using feature temporal derivatives. Feature similarity

is then used to retrieve similar lesions from a database of confirmed cases. To the best of our knowledge this is the first study to use 3D spatio-temporal features extracted from multi-phase CT images in a CBIR framework for FLLs. The rest of the paper is organized as follows. In section II, we describe the evaluation database and the methods used for lesion identification, multi-phase image alignment and 3D feature extraction. Section III illustrates the results and section IV provides a comparative discussion of the proposed framework with existing FLL CBIR systems. We conclude the paper in section V.

II. MATERIALS AND METHOD

A. Materials

Institutional review board approval was obtained for retrospective analysis of 4-phase contrast-enhanced CT images of 30 de-identified patients. CT scans were acquired using a 64-detector SOMATOM sensation scanner (Siemens Medical Solutions, Forchheim, Germany) via a standard 4-phase contrast-enhanced imaging protocol with a slice collimation of $0.6\,mm$, a matrix of 512×512 pixels and an in-plane resolution of $0.59 - 0.78\,mm$. The raw data was reconstructed at an isotropic resolution of $0.6 \times 0.6 \times 0.6\,mm^3$. The evaluation database was constructed using 44 confirmed lesions identified in the 30 patients. The 44 lesions consisted of five types: cyst, hemangioma (HEM), focal nodular hyperplasia (FNH), metastatis (METS), and hepatocellular carcinoma (HCC). There were 14 cases of cyst, 10 cases of HEM, 5 cases of FNH, 11 cases of METS and 4 cases of HCC in the 44 confirmed lesions. One representative lesion was identified in each patient for analysis. The pathology type of the lesions were confirmed based on clinical features, CT scans, data from other imaging modalities and biopsy, wherever needed.

B. Method

The proposed retrieval framework automatically detects candidate FLLs in the CT image [22]. The FLL of interest is then identified in all the four phases using a B-spline-based registration [23]. The FLL is quantitatively represented using 3D spatio-temporal features extracted from various regions within the FLL volume of interest (VOI). A FLL database is constructed using the resulting feature vectors and the corresponding clinical diagnosis. A L2-norm similarity measure between feature vectors of the query lesion and lesions in the database is used for retrieval. The retrieved results are ranked on the basis of similarity score and presented as evidential support to the radiologists. Fig. 1 shows a flowchart of the proposed retrieval framework.

Focal Liver Lesion Identification: We use a hybrid generative-discriminative method proposed in [22] to detect FLLs in a 3D image. The method first uses a generative model to represent non-lesion components such as the healthy liver parenchyma and the enhanced liver vasculature. The candidate FLLs are then identified within the liver volume by eliminating these non-lesion areas. False positives among the identified candidate FLLs are then suppressed using a discriminative approach that uses a lesion-likelihood measure comprising of
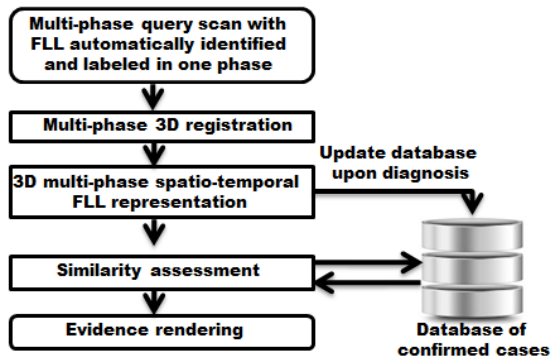
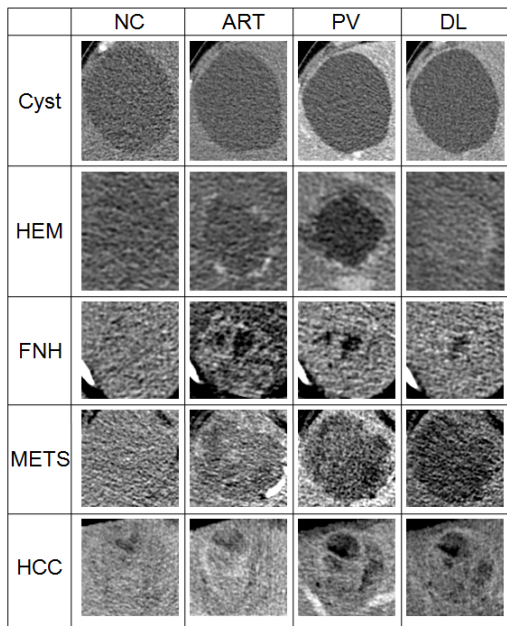Fig. 1: This figure shows a flowchart of the proposed system.

Fig. 2: This figure shows the visual appearance of various lesions over the four phases. Images in a row are from the same lesion; cyst, HEM, FNH, METS and HCC respectively and images in a column belong to the same contrast phase.

three shape-based features: spherical symmetry, compactness and size. All the detected FLLs are presented to an expert who then selects one for further processing.

4-phase Lesion Alignment: FLLs usually do not appear visually distinguishable in all the phases. A FLL is typically detected in the phase in which it shows highest contrast with respect to the liver parenchyma and is localized in the other phases using a non-linear B-spline registration [23].

3D Spatio-Temporal Feature Design and Extraction: Fig. 2 shows evolution of various lesions over different contrast phases. Liver cysts are benign fluid-filled lesions that typically appear as round or oval smooth-edged regions with uniformly low density. Cysts do not show much enhancement after intravenous contrast injection. HEMs exhibit discontinuous nodular peripheral enhancement in the ART phase with centripetal enhancement over time. Central fibrosis and calcification may sometimes be observed due to thrombosis in the vascular channels that makes classification of HEMs challenging. FNH,
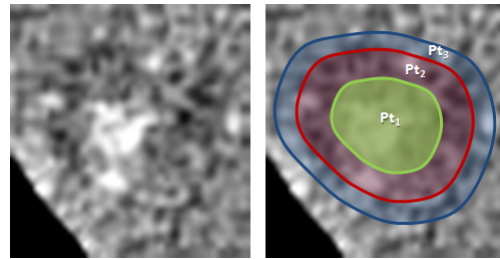

Fig. 3: This figure shows a central calcification inside a HEM. To capture the spatial tissue characteristics we divide the lesion into three partitions.

without any contrast, is usually hypo- or iso-dense to the liver parenchyma. FNH demonstrates bright arterial contrast enhancement except for the central scar; pronounced central arteries may be visible. In the PV phase FNH becomes iso-dense to liver. HEMs and FNHs show similar peripheral enhancement in the ART phase. Also, presence of central abnormalities sometimes make PV washout of HEM and FNH visually similar. METS, on the other hand, is a malignant tumor that usually spreads from other cancer affected organs. METS enhance homogeneously, however, they tend to have less well-defined margins than cysts. METS have a band like peripheral enhancement in ART phase and a washout in DL phase. HCC typically shows ART phase hyper enhancement and washout in either PV or DL phases.

Clinicians primarily use visual patterns generated by contrast intrusion over time to identify FLLs. Spatial visual characteristics such as ring enhancement, nodule-within-a-nodule enhancement, pseudocapsule, central true and pseudo-scars, peripheral washout are fundamental to identifying specific focal lesions [24]. However, accurate FLL classification comes with years of clinical experience. Our goal is to design spatio-temporal image features that perform an objective modeling of the tumors and computationally assist in this classification process. We divide the tumor VOI into three volumetric partitions and extract features from these partitions over the four phases. An example of volumetric partitioning is shown in Fig. 3. The innermost partition, Pt_1, captures central enhancement characteristics caused by structures such as the central scar, fibrosis, calcification, necrosis, if any. The intermediate partition, Pt_2, models the tumor tissue characteristics and the outermost partition, Pt_3 is designed to represent features and the enhancement pattern of the tumor boundary.

We use a standard distance transformation technique based on Euclidean distance to partition the tumor VOI [25]. Distance transformation converts a binary volume into a gray scale volume. The binary volume in our case is the tumor VOI where voxels inside the tumor form the foreground and the rest comprise the background. The tumor is assumed to be segmented either manually or using existing tumor segmentation methods [26], [27]. Distance transformation of this binary volume results in a gray scale volume where each voxel of the gray scale volume represents the distance of that voxel from the closest background voxel in the binary volume. Voxels in the gray scale volume are then grouped into three

partitions based on these distance values.

An additional benefit of tumor partitioning is the computational speed-up. Image features from each partition can now be computed in parallel. In effect the tumor is now partitioned into three sub-volumes and the computation time is governed by the largest of these sub-volumes instead of the entire tumor. In section III we discuss, in detail, the speed-up and enhancement in retrieval performance achieved by tumor partitioning. Large computation time is the primary deterrent to using 3D feature-based retrieval systems in clinical practice. In order to accelerate processing time, instead of extracting features from all voxels within the tumor partitions we perform a uniform sub-sampling of the voxels and use only the selected samples for feature computation. In section III-C a detailed analysis of how the processing time and retrieval performance vary with various amounts of sub-sampling is provided.

Post-partitioning various features such as those based on shape, user-supplied semantics, texture, and intensity can be extracted from the partitions to model the tumor. Shape features are good at distinguishing benign from malignant tumors since benign tumors are well encapsulated as opposed to the malignant ones that often have irregular and visually indistinct boundary. However, shape features have insufficient power to differentiate among benign lesions, or among malignant lesions [15]. Further, since FLLs are most distinctively visible only in one of the phases, temporal change in FLL shape cannot be extracted accurately. In this work our focus is on features that exhibit spatial and temporal evolution, hence we do not employ shape features. User-supplied semantic labels are subjective and often unstructured description of the tumor characteristics with high inter-user variability. Hence, we do not want to use semantic features. Image texture is widely used in the literature to model tumor tissues. Methods that model texture are broadly categorized into statistical and structural approaches. Statistical approaches such as histogram of pixel gray levels and gray level co-occurrence have been found to work best with images whose microtexture can be modeled with a stochastic formulation. Structural approaches such as textons, wavelet transforms and Gabor filters, on the other hand, compute weighted mean of pixel neighborhoods and hence eliminate finer textural details [20], [28]. Published literature reports that gray level density and co-occurrence-based texture features are particularly important to encode local features of hepatic tumors [10], [12], [15], and are most widely used for liver CT image retrieval. Hence, we derive these features from the volumetric partitions and track their temporal evolution over the four phases. We define four 3D feature vectors to model a tumor as defined below.

1) Density Feature: The density feature, F_1, represents the ratio of average pixel intensity inside the partitions to the average pixel intensity of liver parenchyma. F_1 measures lesion enhancement with respect to the surrounding liver tissues and is defined as:

$$F_1 = \{D^{\mathrm{NC}}, D^{\mathrm{ART}}, D^{\mathrm{PV}}, D^{\mathrm{DL}}\}, \qquad (1)$$

where $D^{\mathrm{NC}} = \{d^{\mathrm{NC}}_{\mathrm{Pt}_1}/d^{\mathrm{NC}}_{\mathrm{liver}}, d^{\mathrm{NC}}_{\mathrm{Pt}_2}/d^{\mathrm{NC}}_{\mathrm{liver}}, d^{\mathrm{NC}}_{\mathrm{Pt}_3}/d^{\mathrm{NC}}_{\mathrm{liver}}\}$. $d^{\mathrm{NC}}_{\mathrm{Pt}_i}$ is the average pixel intensity inside Pt_i in the NC phase and $d^{\mathrm{NC}}_{\mathrm{liver}}$ is the average pixel intensity of the healthy liver tissue

in the NC phase. D^{ART}, D^{PV} and D^{DL} are defined in a similar fashion. The resulting density features obtained from all phases are arranged in a 12-dimensional density feature vector. The density feature aims to capture contrast enhancement and washout. For example, if a lesion has $|D^{\mathrm{ART}}| > |D^{\mathrm{NC}}|$ and $|D^{\mathrm{PV}}| < |D^{\mathrm{NC}}|$, then the lesion is enhanced in the ART phase due to contrast propagation and has a washout in the PV phase.

2) Temporal Density Feature: The temporal density feature, F_2, measures temporal enhancement of the lesion in ART, PV and DL phases with respect to the NC phase. It is defined as:

$$F_2 = \{TD^{\mathrm{ART/NC}}, TD^{\mathrm{PV/NC}}, TD^{\mathrm{DL/NC}}\}, \qquad (2)$$

where $TD^{\mathrm{ART/NC}} = \{td^{\mathrm{ART/NC}}_{\mathrm{Pt}_1}, td^{\mathrm{ART/NC}}_{\mathrm{Pt}_2}, td^{\mathrm{ART/NC}}_{\mathrm{Pt}_3}\}$ and for $i = 1, 2, 3$

$$td^{\mathrm{ART/NC}}_{\mathrm{Pt}_i} = \frac{d^{\mathrm{ART}}_{\mathrm{Pt}_i} - d^{\mathrm{NC}}_{\mathrm{Pt}_i}}{d^{\mathrm{NC}}_{\mathrm{Pt}_i}}, \qquad (3)$$

$$td^{\mathrm{PV/NC}}_{\mathrm{Pt}_i} = \frac{d^{\mathrm{PV}}_{\mathrm{Pt}_i} - d^{\mathrm{NC}}_{\mathrm{Pt}_i}}{d^{\mathrm{NC}}_{\mathrm{Pt}_i}}, \qquad (4)$$

$$td^{\mathrm{DL/NC}}_{\mathrm{Pt}_i} = \frac{d^{\mathrm{DL}}_{\mathrm{Pt}_i} - d^{\mathrm{NC}}_{\mathrm{Pt}_i}}{d^{\mathrm{NC}}_{\mathrm{Pt}_i}}. \qquad (5)$$

Similar definitions follow for $TD^{\mathrm{PV/NC}}$ and $TD^{\mathrm{DL/NC}}$. Temporal density features from ART, PV and DL phases are encoded into a 9-dimensional feature vector that models the temporal enhancement of the tumor.

3) Texture Feature: We use a 3D gray level co-occurrence matrix (GLCM) to quantify the gray tone distribution in the tumor sub-volumes. GLCM is an estimation of the joint probability distribution of a pair of gray level voxels. An element $G_{(\theta, d)}(i, j)$ of the GLCM matrix is the probability of the occurrence of gray levels i and j at distance of d from each other along the direction θ. The variables i and j can vary from 1 to N, where N is the number of gray levels in the volume. In 3D, θ can take 26 values resulting from linking a voxel to each of its 26 nearest neighbors. Since directions that are $180°$ apart result in the same co-occurrence matrix, we only consider 13 unique directions. Given an offset d, we compute GLCM over all 13 directions and use the average to make the texture rotation invariant. Offset d is experimentally chosen as described in section III-A.

Six texture coefficients: energy, entropy, inverse difference moment, inertia, cluster shade and correlation as defined in [29] are derived from the rotation invariant GLCM. The texture feature, F_3, is composed as follows:

$$F_3 = \{T^{\mathrm{ART}}, T^{\mathrm{PV}}, T^{\mathrm{DL}}\}, \qquad (6)$$

where $T^{\mathrm{ART}} = \{T^{\mathrm{ART}}_{\mathrm{Pt}_1}, T^{\mathrm{ART}}_{\mathrm{Pt}_2}, T^{\mathrm{ART}}_{\mathrm{Pt}_3}\}$ represents the texture features derived from the three partitions in the ART phase. $T^{\mathrm{ART}}_{\mathrm{Pt}_i} = \{t^{\mathrm{ART}}_{1_{\mathrm{Pt}_i}}, \ldots, t^{\mathrm{ART}}_{6_{\mathrm{Pt}_i}}\}$ where $t^{\mathrm{ART}}_{k_{\mathrm{Pt}_i}}$'s, $k = \{1, \ldots, 6\}$, are computed as defined in Table I from the GLCM of Pt_i in the ART phase. Similar definition applies for T^{PV} and T^{DL}. The resulting texture coefficients from nine partitions in ART, PV and DL phases are arranged into a 54-dimensional feature vector which encodes the tumor texture.

TABLE I: This table describes the texture coefficients derived from the GLCM matrix. The term $g(i,j)$ represents the joint probability density of the gray level pair (i,j).

Texture Coefficient	Expression and Qualitative Analysis
Energy	$t_1 = \sum_{i=0}^{N-1} \sum_{j=0}^{N-1} g(i,j)^2$ Energy quantifies the repetition of gray level pairs in an image.
Entropy	$t_2 = \sum_{i=0}^{N-1} \sum_{j=0}^{N-1} g(i,j) log_2(g(i,j))$ Entropy represents the randomness in the image.
Inverse Difference Moment	$t_3 = \sum_{i=0}^{N-1} \sum_{j=0}^{N-1} \frac{1}{1+(i-j)^2} g(i,j)$ Inverse difference moment measures the local homogeneity in the image.
Inertia	$t_4 = \sum_{i=0}^{N-1} \sum_{j=0}^{N-1} (i-j)^2 g(i,j)$ Inertia gauges local variations in an image.
Cluster Shade	$t_5 = \sum_{i=0}^{N-1} \sum_{j=0}^{N-1} (i+j-\mu_i-\mu_j)^3 g(i,j)$ where, $\mu_i = \sum_{i=0}^{N-1} i \sum_{j=0}^{N-1} g(i,j)$, and $\mu_j = \sum_{j=0}^{N-1} j \sum_{i=0}^{N-1} g(i,j)$. Cluster shade quantifies perceptual uniformity and proximity.
Correlation	$t_6 = \sum_{i=0}^{N-1} \sum_{j=0}^{N-1} \frac{(i-\mu_i)(j-\mu_j)g(i,j)}{\sigma_i \sigma_j}$ where, $\sigma_i = \sum_{i=0}^{N-1} (i-\mu_i)^2 \sum_{j=0}^{N-1} g(i,j)$, and $\sigma_j = \sum_{j=0}^{N-1} (j-\mu_j)^2 \sum_{i=0}^{N-1} g(i,j)$. Correlation assesses the linearity of relationship between various gray level pixel pairs.

4) Temporal Texture Feature: Temporal texture, F_4, is defined as the normalized difference in texture at the three enhancement phases. F_4 is formulated as:

$$F_4 = \{TT^{\text{ART}}, TT^{\text{PV}}, TT^{\text{DL}}\}, \tag{7}$$

where, $TT^{\text{ART}} = \{TT^{\text{ART}}_{\text{Pt}_1}, TT^{\text{ART}}_{\text{Pt}_2}, TT^{\text{ART}}_{\text{Pt}_3}\}$ is the temporal texture in the ART phase formulated as derivative of the six texture coefficients in each partition in the ART phase; $TT^{\text{ART}}_{\text{Pt}_i} = \{tt^{\text{ART}}_{1\text{Pt}_i}, \ldots, tt^{\text{ART}}_{6\text{Pt}_i}\}$, $i = \{1,2,3\}$. Derivative of each texture coefficient is defined as:

$$tt^{\text{ART}}_{k_{\text{Pt}_i}} = \frac{t^{\text{ART}}_{k_{\text{Pt}_i}} - \displaystyle\underset{\mathcal{P}\in\{\text{ART},\text{PV},\text{DL}\}}{\text{median}} t^{\mathcal{P}}_{k_{\text{Pt}_i}}}{\displaystyle\underset{\mathcal{P}\in\{\text{ART},\text{PV},\text{DL}\}}{\max} t^{\mathcal{P}}_{k_{\text{Pt}_i}} - \underset{\mathcal{P}\in\{\text{ART},\text{PV},\text{DL}\}}{\min} t^{\mathcal{P}}_{k_{\text{Pt}_i}}} \tag{8}$$

for $k = 1, \ldots, 6$. Texture derivative in PV and DL phases, TT^{PV} and TT^{DL} respectively, are formulated analogously with the individual texture coefficient derivatives defined as:

$$tt^{\text{PV}}_{k_{\text{Pt}_i}} = \frac{t^{\text{PV}}_{k_{\text{Pt}_i}} - \displaystyle\underset{\mathcal{P}\in\{\text{ART},\text{PV},\text{DL}\}}{\text{median}} t^{\mathcal{P}}_{k_{\text{Pt}_i}}}{\displaystyle\underset{\mathcal{P}\in\{\text{ART},\text{PV},\text{DL}\}}{\max} t^{\mathcal{P}}_{k_{\text{Pt}_i}} - \underset{\mathcal{P}\in\{\text{ART},\text{PV},\text{DL}\}}{\min} t^{\mathcal{P}}_{k_{\text{Pt}_i}}}, \tag{9}$$

$$tt^{\text{DL}}_{k_{\text{Pt}_i}} = \frac{t^{\text{DL}}_{k_{\text{Pt}_i}} - \displaystyle\underset{\mathcal{P}\in\{\text{ART},\text{PV},\text{DL}\}}{\text{median}} t^{\mathcal{P}}_{k_{\text{Pt}_i}}}{\displaystyle\underset{\mathcal{P}\in\{\text{ART},\text{PV},\text{DL}\}}{\max} t^{\mathcal{P}}_{k_{\text{Pt}_i}} - \underset{\mathcal{P}\in\{\text{ART},\text{PV},\text{DL}\}}{\min} t^{\mathcal{P}}_{k_{\text{Pt}_i}}}. \tag{10}$$

Texture derivatives computed for the three enhanced phases are organized into a 54-dimensional temporal texture feature vector that represents the textural evolution of the tumor. The four feature vectors F_1, F_2, F_3 and F_4 form the FLL model.

Since we use GLCM-based texture features in this paper, it turns out that we can further improve tumor processing speed by reducing the number of gray levels used while populating the GLCM matrix. An element (i,j) of the GLCM matrix measures the probability of co-occurrence of gray level pairs i and j. Computing 3D GLCM in 13 directions using the original CT values is highly expensive both computationally and in terms of memory requirement. We quantize down the original CT values to fewer distinct gray levels in order to reduce the size and computation time of the GLCM. Optimum number of gray levels can be determined experimentally. Section III-C provides analysis of gain in computation time versus retrieval performance for various gray level counts.

Similarity Assessment and Evidence Rendering: Similarity between a query FLL and the model FLLs in the database can be measured using a L^2 distance between the respective feature vectors. Distance between two lesions FLL$_1$ and FLL$_2$ in L^2 is defined as:

$$D_{L^2}(\text{FLL}_1, \text{FLL}_2) = \sum_{i=1}^{4} w_i ||F^i_{\text{FLL}_1} - F^i_{\text{FLL}_2}||_{L^2}. \tag{11}$$

The term $F^i_{\text{FLL}_1}$ represents the ith feature vector of FLL$_1$ where i iterates over density, temporal density, texture and temporal texture feature vectors and w_i is the respective weight. Weight selection is elaborated in section III-A.

Model FLLs in the database are sorted in increasing order of their distance to the query FLL and the closest matching FLLs are rendered to the radiologist. It is possible to predict the pathological type of the query FLL using BEP. BEP is defined for each query as the percentage of correct retrievals with respect to the query FLL's class within the top $2C$ results where C is the size of the query FLL's class [30]. The query FLL is predicted to belong to the class that has the highest BEP score as follows:

$$\text{Query} \subseteq \mathcal{C}_i$$
$$\text{if, } \text{BEP}(\mathcal{C}_i) = \max_{k=1,2,\ldots,5}(\text{BEP}(\mathcal{C}_k)) \tag{12}$$

where $\mathcal{C}_k$ represents the kth class of FLL pathology in the database. The term $\text{BEP}(\mathcal{C}_i)$ represents the BEP score when query FLL is assumed to belong to class $\mathcal{C}_i$. The distance of the query FLL to a class $\mathcal{C}_k$ can be computed using average distance to model FLLs belonging to class $\mathcal{C}_k$ retrieved within the top $2|\mathcal{C}_k|$ results as formulated below:

$$\text{Distance}(\mathcal{C}_k) = \frac{1}{\text{N}_{\mathcal{C}_k}} \sum_{i=1}^{\text{N}_{\mathcal{C}_k}} D_{L^2}(\text{FLL}_{\text{Query}}, \text{FLL}_i), \tag{13}$$

where $\text{N}_{\mathcal{C}_k}$ is the number of FLLs belonging to class $\mathcal{C}_k$ retrieved in the top $2|\mathcal{C}_k|$ results.
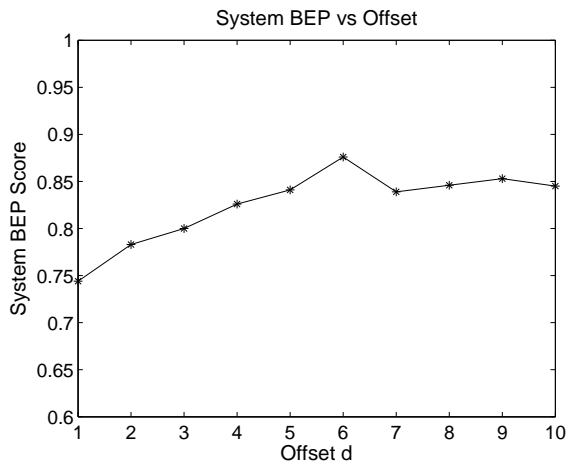
Fig. 4: This figure plots the system BEP score for various values of offsets. The offset, d, is the distance between gray level pairs used for computing GLCM entries.

Fig. 5: This plot shows the variation in tumor volume (in cm^3) for the five tumor classes in the database.

Although a CBIR system can predict the pathological type of an unknown lesion, the primary contribution of a CBIR system in the clinical routine is its capability of providing evidential support in favor and also against its prediction. It is important for radiologists to not only look at examples of similar lesions from the same pathology type but also refer to visually similar lesions belonging to a different class of pathology for a possible differential diagnosis.

III. EXPERIMENTS AND RESULTS

The proposed CBIR framework is evaluated on a database of 44 FLLs identified in 30 patients and comprising of five pathological types. One representative FLL is chosen from each patient for analysis. Precision-recall curve and BEP score are used to evaluate the retrieval performance of the proposed framework. Precision is defined as the ratio of retrieved lesions that belong to the query class with respect to the total number of lesions retrieved[1] and recall is defined as the ratio of number of retrieved lesions that belong to the query class with respect to all model lesions in the database that belong to the query class. Leave-one-out cross validation scheme is used to compute the precision-recall curves and the BEP scores.

A. Parameter Optimization

In this section we describe selection of offset (distance between gray level pairs while computing GLCM) and feature weights (used for inter-lesion comparison) respectively.

Offset: We compare the retrieval performance at various values of offsets, d, by computing texture and temporal texture features from GLCM at $d = 1, 2, \ldots, 10$, and measuring the corresponding system BEP scores (Fig. 4). Higher offsets produce better results, albeit, using a smaller subset of the dataset. Large offsets cannot be used to model small tumors. In our framework we first partition a tumor into three sub-volumes

---

[1] This definition of precision is used in the field of information retrieval and is not equal to the one used in other areas of science and technology.
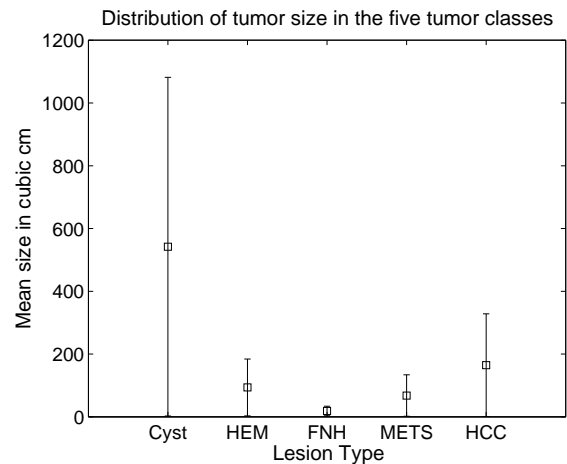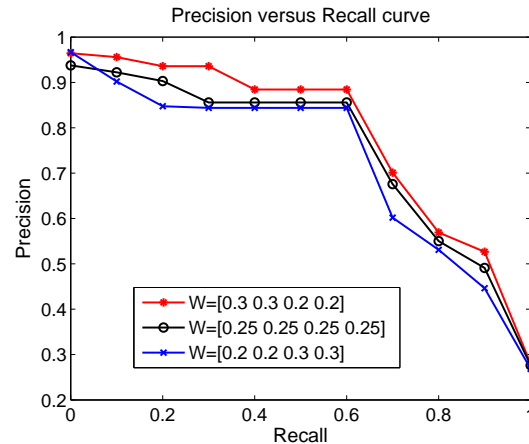

Fig. 6: This figure plots precision versus recall curves for different feature weight vectors. Precision-recall curves for optimal and equal weight vectors are observed to be close.

and then extract the GLCM matrix from each individual sub-volume. If the offset value is too large then GLCM for the sub-volumes of small tumors remain very sparsely populated or empty. Hence, with high offset it is not possible to model small tumors. The results reported with higher offsets include only the big tumors which could be a reason for better system performance. In Fig. 5 we plot tumor size distribution for the five classes of lesions in our database. From experiments we observe that a maximum offset of four is able to model all the tumors in our database and hence for subsequent analysis we set $d = 4$.

Feature Weights: Similarity between two lesions is assessed using a weighted L^2 difference between the respective feature vectors (Eq. 11). To compute the optimum weights, we conduct a brute-force search where the objective is to maximize the system BEP score under an increment/ decrement of the weights in steps of 0.05 while keeping their sum equal to one. It is found that a weight vector of $[0.3\,0.3\,0.2\,0.2]$ generates the best results. Fig. 6 compares precision-recall curves for various weights including the optimal and equal weight vectors.
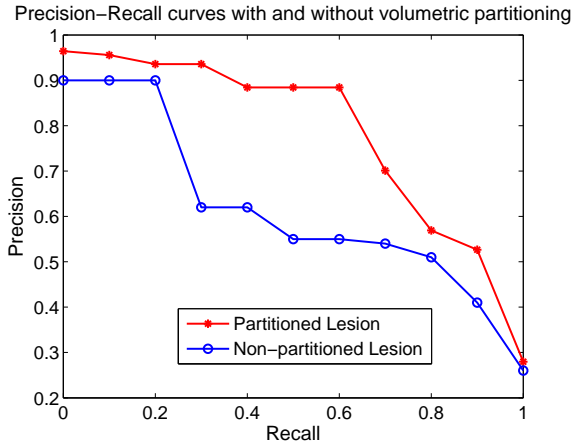
Fig. 7: This figure compares precision-recall curves when the lesions in the database are volumetrically partitioned into three sub-volumes versus when they are not. The retrieval performance obtained by non-partitioned lesions is found to be inferior to that obtained by partitioned lesion representation.

TABLE II: This table enlists the Bull's Eye Percentage for various lesion classes.

Lesion Class	Bull's Eye Percentage Score
Cyst	0.87
HEM	0.62
FNH	0.70
METS	0.94
HCC	1.00

B. Tumor Partitioning

As mentioned in section II-B, we divide the tumor into partitions and extract features from each partition to capture the spatio-temporal characteristics of the tumor. Fig. 7 shows the gain in retrieval performance obtained by dividing the tumor into three partitions against the case when tumors are represented by features extracted from the whole VOI. Retrieval performance post-partitioning is clearly superior to the non-partitioned case.

C. Retrieval Performance and Processing Speed

Fig. 7 plots the retrieval performance of the proposed retrieval framework in terms of precision and recall. The system's precision remains above 0.85 till a recall of 0.6. The BEP score for the five lesion pathologies is tabulated in Tab. II. The global mean score of 82.6% demonstrates good discriminatory properties of the 3D spatio-temporal features. A more detailed examination of the results shows excellent BEP scores, between 87% and 100%, for cyst, METS and HCC. This can be contributed to the markedly different temporal enhancement of these three lesion types. The low number of HCCs in our database may have led to a perfect BEP score for HCC. For a more thorough evaluation we would like to test the performance with a wider example set of HCC. HEM and FNH, however, report lower BEP scores. Pt_3, which captures the peripheral enhancement, tends to show similar
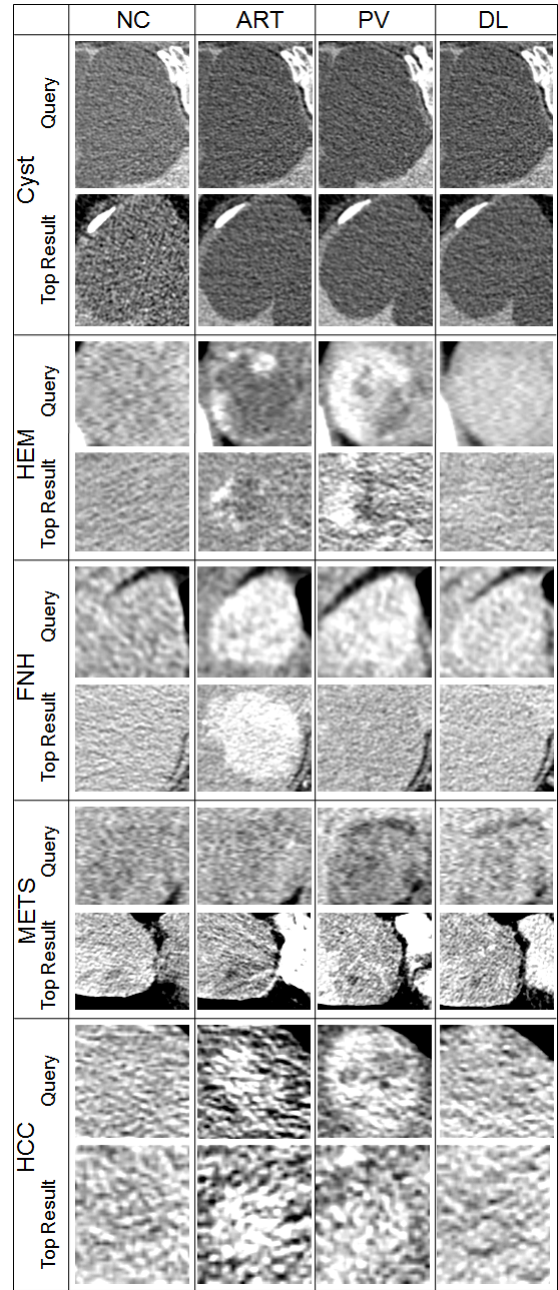

Fig. 8: This figure shows the top retrieval results for five query lesions, one from each of the five lesion classes.

enhancement in ART phase for both HEM and FNH. Further, Pt_1 shows similar temporal washout in the DL phase for both HEM and FNH due to the occasional presence of a central scar in FNH. This may explain why lower scores are obtained for HEM and FNH. FNH is difficult to detect and it is well known clinically that they are called "stealth lesions" if the ART phase enhancement is not well demonstrated.

Fig. 8 shows the top retrieval results for five query lesions, one from each of the five lesion classes. For 98% of query lesions, at least one lesion of the same pathological type as the query lesion is rendered in the top two retrieval results.

Low query processing time is critical for the clinical feasibility of a retrieval system. Various characteristics of
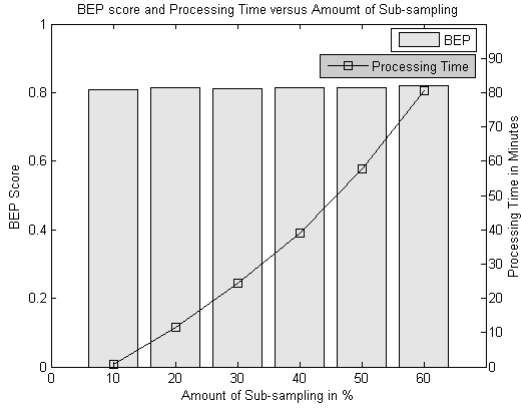
Fig. 9: This figure plots the BEP scores and the processing times for various amounts of volumetric sub-sampling.
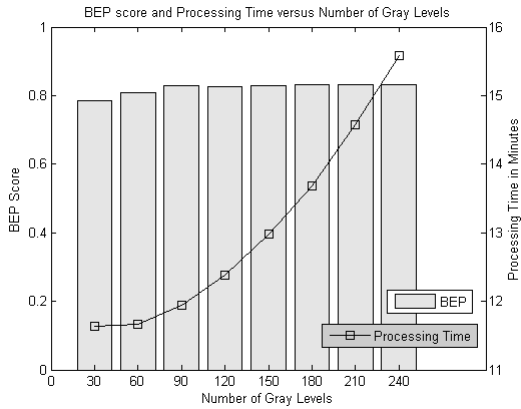

Fig. 10: This figure plots the BEP scores and the processing times for various counts of distinct gray levels.

TABLE III: This table compares the processing times for some FLLs when tumor partitioning, volumetric sub-sampling and gray level quantization are used to accelerate feature computation versus when no acceleration is used. For acceleration we use 25% sub-sampling and 60 gray levels.

FLL Size (in cm^3)	Processing time with acceleration (in min.)	Processing time without without acceleration (in min.)
69.6	0.08	2.41
133.6	0.19	5.34
184.1	0.26	7.66
286.4	0.33	8.95
328.1	0.46	12.84

accuracy. Fig. 10 plots the system BEP score versus number of gray levels used for feature computation. Total time taken to compute 3D features for all lesions in the database is also plotted against the number of gray levels. As expected, higher number of gray levels increases the computation time, however, the gain in performance saturates after certain gray levels. In this paper we use 60 gray levels for feature extraction.

Tab. III compares the processing times for some FLLs with and without net computation acceleration obtained by tumor partitioning, volumetric sub-sampling and gray level quantization. On an average the computation with acceleration is more than 28 times faster than without acceleration.

IV. DISCUSSION

A. System Comparison

In this paper we propose a retrieval framework for FLL characterization using 3D image-based spatio-temporal features. To the best of our knowledge no FLL CBIR system based on 3D multi-phase features have been reported in the literature. The closest related works have studied lesion retrieval based on 2D features derived from representative slices of single or multi-phase CT images [13], [14], [15], [16], [17]. In the following paragraphs we compare the proposed system with these prior studies in detail.

Yu *et al.* in [13] propose retrieval of three types of FLLs: cyst, HEM, and HCC using BoW and 2D image-based features. The lesions are spatially partitioned and BoW histograms are computed for each partition. The visual vocabulary for BoW histogram is constructed using image patches of the training lesions without normalization. Additionally 93 image-based global features are constructed from the unpartitioned tumor region of interest based on intensity, GLCM, Gabor filter and tumor shape. The lesion is represented by averaging spatial BoW and global image-based features across multiple phases. A mean average retrieval precision of 88% is reported. In an extension to this work, the authors in [14] eliminate lesion partitioning and use distance metric learning methods to compute similarity between global BoW histograms and report an average precision of above 90% when evaluated on a database of cyst, HEM and hepatomas. Processing time, however, is not reported. In [13] lesion spatial-partitioning is used, though only to construct the BoW histograms. For other image-based features no spatial information is preserved.

our feature extraction framework contribute towards accelerating query processing time. Tumor partitioning is the first contributor. By partitioning the tumor we process all sub-volumes concurrently in a multi-core computing framework. The processing time is now governed by the largest sub-volume instead of the entire tumor volume.

Further, we perform sub-sampling of the sub-volumes instead of using all voxels during feature computation. Fig. 9 shows how the system BEP score and the total feature computation time for *all* lesions in the database vary with varying amounts of sub-sampling. The computation time is measured using MATLAB R2011b without any GPU acceleration in an Intel Xeon 2.4 GHz 4 core processor with 6 GB RAM. We observe that BEP score varies from 0.80 to 0.82 with additional sampling, however, gain in speed-up is substantial when lower number of voxels are sampled. In this paper we use 25% sub-sampling to compute features.

Use of GLCM for texture computation gives us another parameter to gain additional speed-up, namely, the number of distinct gray levels used for GLCM computation. Larger the number of distinct gray levels, bigger is the GLCM matrix and hence slower is the computation. We quantize down the original CT gray levels to a lower number of distinct values and study its effect on the computation time and the retrieval

Further averaging BoW and image features over multiple phases leads to loss of temporal information. In [14] both spatial and temporal information is neglected for BoW and image features. Pathologically different lesions may appear visually similar in some phases. By combining features from various phases, a good correspondence between lesions in sequential phases is not guaranteed. Similar sequential evolution of two lesions is essential for them to be categorized to the same pathological type. Further, from experiments we observe that computing GLCM texture features over the whole tumor without acceleration is slow. Research shows that computing texture using Gabor filter is even slower than GLCM [20]. We propose a much simpler modeling of tumors using density and only six GLCM-based texture coefficients that preserve both spatial and temporal characteristics of the tumor and are also faster to compute as against the elaborate modeling of tumors proposed in [13], [14] using 93 features and BoW learning. When evaluated using cyst, HEM and HCC, our system achieves a higher mean average precision of 92.4%.

In [15], the authors design a FLL retrieval framework using GLCM-based 2D temporal features derived from multi-phase CT images. The features are, however, derived by averaging density and texture over a tumor bounding box. The system is tested on a database of 69 FLLs comprising of six pathological types. A BEP score of 78% is obtained. It is reported that for 90% query lesions, the processing time is more than 10 minutes. 2D GLCM captures the joint probability distribution of gray level pairs in only 4 directions: $0°, 45°, 90°$, and $135°$. However, a 3D GLCM represents gray level distribution in 13 directions along the 13 neighbors of a voxel. Averaging 2D features over multiple slices does not accurately approximate the 3D texture. Further, by averaging features over the whole bounding box, authors dismiss the spatial enhancement characteristics of the tumor. In this paper we use 3D regionally-partitioned temporal features and obtain a superior precision-recall curve and a higher system BEP score than in [15] with more than 20 times faster processing speed.

A CBIR system is proposed in [16] to differentiate cyst from METS using radiological semantic labels and computer-generated features based on density histogram and its moments obtained from three orthogonal 2D cuts of a single-phase scan volume. A random forest classifier is used to learn a discriminant distance between various FLL attributes. The classification performance is measured using a receiver operating characteristic curve. The framework proposed in [16] uses only global density-based features derived from the lesion area and the whole liver in a single contrast phase. Moments are well-known quantitative measures of the global shape of a set of points. FLL shapes, however, are rarely used to differentiate different lesions in the clinical routine. This may explain why inferior results are obtained using moments as the discriminating features of the FLLs.

In [17], the authors propose retrieval of cyst, METS and HEM using only a single image in the PV phase on a database of 30 images. Computer-generated image-based features and higher level radiological semantic labels are used to represent a FLL. Visual similarity between each pair of lesions is adjudged by two senior radiologists based on texture, boundary shape
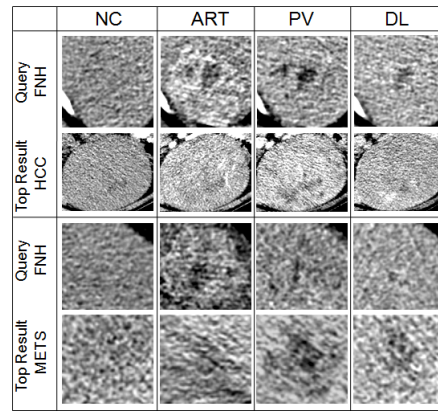

Fig. 11: This figure shows some cases where the top retrieved lesion does not belong to the query lesion class.

and boundary sharpness. The similarity measure between two FLLs is defined as $3/2/1$ for very similar, somewhat similar and not similar pairs respectively. The system is evaluated in terms of precision and recall on how well the system retrieves visually similar lesions in comparison to radiology experts. A mean precision greater than 90% is achieved. The retrieval framework proposed in [17] is optimized and characterized for retrieving visually similar lesions as perceived by expert radiologists as opposed to retrieving lesions belonging to the same lesion class. Retrieval performance in terms of FLL characterization is not reported which makes a formal performance comparison with our system difficult. Further, only one slice in the PV phase, selected manually, is used for feature computation. Higher level radiological annotations that are inherently known to be subjective and widely user-dependent are used to bridge the performance gap.

B. System Performance

For most cases the proposed CBIR system ranks lesions belonging to the same pathological type as the query lesion higher than lesions from other pathological groups. However, in certain cases lesions from a different lesion class may be ranked higher as shown in Fig. 11. This is due to variation in visual appearance among lesions belonging to the same pathological group. In clinical practice other higher level semantic information and clinical history are used to distinguish such cases. In this paper we do not use any semantic information. However, we try to model commonly used semantic descriptions such as relative density of tumor region with respect to the liver parenchyma and tumor edge characteristics using image-based features. Nonetheless, in future we would like to explore other features that are more efficient in distinguishing visually similar lesions from different pathological classes.

C. Clinical Feasibility

By reducing query computation time, the proposed framework establishes the clinical feasibility of 3D feature-based CBIR systems. However, at present we do not have a graphical user interface for easy use of the system by radiologists.

Design of a good user interface poses its own set of technical challenges. These need to be addressed before clinical deployment of the system is possible.

V. Conclusion

In this paper we propose a FLL CBIR framework using 3D spatio-temporal features derived from 4-phase contrast-enhanced CT images. Acceleration techniques are employed to speed up the 3D feature extraction process, known to be the primary bottleneck in integration of 3D feature-based retrieval systems into the clinical routine. The proposed system is evaluated in terms of precision-recall and system BEP score on a database of 44 lesions comprising of five pathological categories. The proposed system performs better and faster than existing 2D feature-based FLL CBIR systems.

In future work, we would like to conduct a clinical validation of the proposed system and evaluate the system's performance on a larger database that includes more FLL pathologies. We acknowledge that the database used in this paper, though at par with some of the existing studies [15], [17], is small. A systematic search on the intrinsic dimensionality of the database will be a future addition to this work. CBIR systems are known to improve radiological diagnostic accuracy [15], however, high processing times have rendered their integration into the clinical routine impractical. By keeping the query processing time low and including more pathological cases we hope to be able to integrate the proposed system as a diagnostic assistant into the routine radiological practices.

Acknowledgment

References

[1] H. Ji, J. D. McTavish, K. J. Mortele, W. Wiesner, and P. R. Ros, "Hepatic imaging with multidetector CT," *Radiographics*, vol. 21, no. suppl 1, pp. S71-S80, 2001.

[2] R. Lencioni, D. Cioni, and C. Bartolozzi, "Focal liver lesions: detection, characterization, ablation," *Springer*, 2005.

[3] I. R. Kamel, M. A. Choti, K. M. Horton, H. J. V. Braga, B. A. Birnbaum, E. K. Fishman, R. E. Thompson, and D. A. Bluemke, "Surgically staged focal liver lesions: accuracy and reproducibility of dual-phase helical CT for detection and characterization," *Radiology*, vol. 227, no. 3, pp. 752-757, 2003.

[4] I. R. Francis, R. H. Cohan, N. J. McNulty, J. F. Platt, M. Korobkin, A. Gebremariam, and K. Ragupathi, "Multidetector CT of the liver and hepatic neoplasms: effect of multiphasic imaging on tumor conspicuity and vascular enhancement," *Am. J. Roentgenol.*, vol. 180, no. 5, pp. 1217-1224, 2003.

[5] H. J. Kim, A. Y. Kim, T. K. Kim, J. H. Byun, H. J. Won, K. W. Kim, Y. M. Shin, P. N. Kim, H. K. Ha, and M. G. Lee, "Transient hepatic attenuation differences in focal hepatic lesions: dynamic CT features," *Am. J. Roentgenol.*, vol. 184, no. 1, pp. 83-90, 2005.

[6] H. Muller, N. Michoux, D. Bandon, and A. Geissbuhler, "A review of content-based image retrieval systems in medical applications - clinical benefits and future directions," *Int. J. Med. Inform.*, vol. 73, no. 1, pp. 1-23, 2004.

[7] C. B. Akgul, D. L. Rubin, S. Napel, C. F. Beaulieu, H. Greenspan, and B. Acar, "Content-based image retrieval in radiology: current status and future directions," *J. Digit. Imaging*, vol. 274, no. 2, pp. 208-222, 2011.

[8] L. R. Long, S. Antani, R. M. Deserno, and G. R. Thoma, "Content-based image retrieval in medicine: retrospective assessment, state of the art, and future directions," *International Journal of Healthcare Information Systems and Informatics*, vol. 4, no. 1, pp. 1-16, 2009.

[9] M. Gletsos, S. G. Mougiakakou, G. K. Matsopoulos, K. S. Nikita, A. S. Nikita, and D. Kelekis, "A computer-aided diagnostic system to characterize CT focal liver lesions: design and optimization of a neural network classifier," *IEEE Trans. Inf. Technol. Biomed.*, vol. 7, no. 3, pp. 153-162, 2003.

[10] G.-M. Xian, "An identification method of malignant and benign liver tumors from ultrasonography based on GLCM texture features and fuzzy SVM," *Expert Sys. Appl.*, vol. 37, no. 10, pp. 6737-6741, 2010.

[11] S. G. Mougiakakou, I. K. Valavanis, A. Nikita, and K. S. Nikita, "Differential diagnosis of CT focal liver lesions using texture features, feature selection and ensemble driven classifiers," *Artif. Intell. Med.*, vol. 41, no. 1, pp. 25-37, 2007.

[12] M. Yu, Z. Lu, Q. Feng, and W. Chen, "Liver CT image retrieval based on non-tensor product wavelet," *Proc. of International Conference on Medical Image Analysis and Clinical Applications*, pp. 67-70, 2010.

[13] M. Yu, Z. Lu, Q. Feng, and W. Chen, "Extraction of lesion-partitioned features and retrieval of contrast-enhanced liver images," *Comput. Math. Methods Med.*, vol. 2012, 2012.

[14] W. Yang, Z. Lu, M. Yu, M. Huang, Q. Feng and W. Chen, "Content-based retrieval of focal liver lesions using bag-of-visual-words representations of single- and multiphase contrast-enhanced CT images," *J. Digit. Imaging*, vol. 25, pp. 708-719, 2012.

[15] Y. Chi, J. Zhou, S. K. Venkatesh, Q. Tian, and J. Liu, "Content-based image retrieval of multiphase CT images or focal liver lesion characterization," *Med. Phy.*, vol. 40, no. 10, article ID 103502, 2013.

[16] M. Costa, A. Tsymbal, M. Hammon, A. Cavallaro, M. Suhling, S. Seifert, and D. Comaniciu, "A discriminative distance learning-based CBIR framework for characterization of indeterminate liver lesions," *Medical Content-Based Retrieval for Clinical Decision Support*, LNCS 7075, pp. 92-104, 2012.

[17] S. A. Napel, C. F. Beaulieu, C. Rodriguez, J. Cui, J. Xu, D. Korenblum, H. Greenspan, Y. Ma, and D. L. Rubin, "Automated retrieval of CT images of liver lesions on the basis of image similarity: method and preliminary results," *Radiology*, vol. 256, no. 1, pp. 243-252, 2010.

[18] J. L. Sobel, M. L. Pearson, K. Gross, and others, "Information content and clarity of radiologists' reports for chest radiography," *Acad. Radiol.*, vol. 3, no. 9, pp. 709-717, 1996.

[19] M. J. Stoutjesdijk, J. J. Futterer, C. Boetes, L. E. Van Die, G. Jager, and J. O. Barentsz, "Variability in the description of morphologic and contrast enhancement characteristics of breast lesions on magnetic resonance imaging," *Invest. Radiol.*, vol. 40, no. 6, pp. 355-362, 2005.

[20] Y. Qian, X. Gao, M. Loomes, R. Comley, B. Barn, R. Hui, and Z. Tian, "Content-based retrieval of 3D medical images," *Proc. of the third International Conference on eHealth, Telemedicine, and Social Medicine*, pp. 7-12, 2011.

[21] A. Burner, R. Donner, M. Mayerhoefer, M. Holzer, F. Kainberger, and G. Langs, "Texture Bags: Anamoly retrieval in medical images based on local 3D-texture similarity," *Medical Content-Based Retrieval for Clinical Decision Support. Springer Berlin Heidelberg*, pp. 116-127, 2012.

[22] Y. Chi, J. Zhou, S. K. Venkatesh, S. Huang, Q. Tian, and J. Liu, "Computer-aided focal liver lesion detection," *Int. J. Compt. Assist. Radiol. Surg.*, vol. 8, no. 4, pp 511-525, 2013.

[23] P. A. Yushkevich, J. Piven, H. C. Hazlett, R. G. Smith, S. Ho, J. C. Gee, and G. Gerig, "User-guided 3D active contour segmentation of anatomical structures: significantly improved efficiency and reliability," *Neuroimage*, vol. 31, no. 3, pp. 1116-1128, 2006.

[24] K. M. Elsayes, V. R. Narra, Y. Yin, G. Mukundan, M. Lammle, and J. J. Brown, "Focal hepatic lesions: diagnostic value of enhancement pattern approach with contrast-enhanced 3D gradient-echo MR imaging," *Radiographics*, vol. 25, no. 5, pp. 1299-1320, 2005.

[25] A. Rosenfeld and J. L. Pfaltz, "Sequential operations in digital picture processing," *J. ACM*, vol. 13, no. 4, pp. 471-494, 1996.

[26] S. -J. Park, K. -S. Seo, and J. -A. Park, "Automatic hepatic tumor segmentation using statistical optimal threshold," *Computational Science - ICCS 2005*, vol. 3514, pp. 934-940, 2005.

[27] L. Massoptier and S. Casciaro, "A new fully automatic and robust algorithm for fast segmentation of liver tissue and tumors from CT scans," *Eur. Radiol.*, vol. 18, no. 8, pp. 1658-1665, 2008.

[28] T. Maenpaa and M. Pietikainen, "Texture analysis with local binary patterns," *Handbook of Pattern Recognition and Computer Vision 3*, pp. 197-216, 2005.

[29] R. M. Haralick, K. Shanmugam, and I. Dinstein, "Textural features for image classification," *IEEE Trans. Syst. Man Cybern.*, vol. 3, no. 6, pp. 610-621, 1973.

[30] B. S. Manjunath, "Introduction to MPEG-7: Multimedia content description interface," *Wiley*, 2002.